nature communications

Article

https://doi.org/10.1038/s41467-025-56671-7

Advancing Ag_2Se thin-film thermoelectrics via selenization-driven anisotropy control

Received: 13 October 2024

Accepted: 27 January 2025

Published online: 12 February 2025

Check for updates

Tianyi Cao[1], Xiao-Lei Shi[1] ✉, Boxuan Hu[1], Qishuo Yang[1,2], Wan-Yu Lyu[1], Shuai Sun[1], Liang-Cao Yin[3], Qing-Yi Liu[1], Wenyi Chen[2], Xiaodong Wang[4], Siqi Liu[1], Meng Li[1], Wei-Di Liu[1], Tuquabo Tesfamichael[5], Qingfeng Liu[3], Jennifer MacLeod[1] & Zhi-Gang Chen[1] ✉

The debate over the optimal orientation of Ag_2Se thin films and its influence on thermoelectric performance remains ongoing. Here, we report a wet-chemical selenization-based anisotropy optimization technique to control the in-plane orientation of the Ag_2Se thin film, steering it away from (002) nearly parallel planes that hinder charge carrier mobility. This approach enables us to achieve an impressive power factor of 30.8 μW cm^{-1} K^{-2} at 343 K. The as-fabricated Ag_2Se thin film demonstrates remarkable durability, retaining over 90% of its power factor after six months of air exposure, and outstanding flexibility, with performance variation staying within 5% after 2000 bending cycles at a 5 mm radius. These attributes are attributed to the controlled film thickness, crystallinity, and strong adhesion to the polyimide substrate. Additionally, the as-assembled slotted thermoelectric device delivers an output power of 0.58 μW and a competitive power density of 807 μW cm^{-2} at a temperature difference of 20 K, alongside a high normalized power density of 1.8 μW cm^{-2} K^{-2}, highlighting its potential for practical application. This study provides valuable insights into the design of high-performance, highly flexible thermoelectric thin films for real-world applications.

Flexible thermoelectric technology can convert the temperature difference between the human body and the environment into electricity by the Seebeck effect, offering a potential solution to the challenge of providing a lightweight, safe, and sustainable power source for wearable electronics[1–3]. To improve the thermoelectric conversion efficiency, it is crucial to optimize the thermoelectric properties of the materials[2]. The thermoelectric performance is generally evaluated using the figure-of-merit (ZT), which can be expressed as $ZT = \frac{S^2\sigma}{\kappa}T = \frac{S^2\sigma}{\kappa_e+\kappa_l}T$, where S is the Seebeck coefficient, σ is the electrical conductivity, $S^2\sigma$ is the power factor, κ is the thermal conductivity, κ_e is the electronic thermal conductivity, κ_l is the lattice thermal conductivity, and T is the absolute temperature[4]. Since the S, σ, and κ_e are directly coupled with the carrier concentration (n), tuning the n is effective for optimizing the overall thermoelectric performance. To achieve this goal, historically, doping has been used to manipulate the band structure[5], and introducing secondary phases can stimulate the energy filtering effect[6], effectively decoupling the S, σ, and κ_e, thereby improving the ZT value. The κ_l is typically associated with phonons. Crystal and lattice defects introduce additional scattering centers into the phonon transport path, causing phonons with

[1]School of Chemistry and Physics, ARC Research Hub in Zero-emission Power Generation for Carbon Neutrality, and Centre for Materials Science, Queensland University of Technology, Brisbane, QLD, Australia. [2]School of Mechanical and Mining Engineering, The University of Queensland, Brisbane, QLD, Australia. [3]State Key Laboratory of Materials-Oriented Chemical Engineering, College of Chemical Engineering, Nanjing Tech University, Nanjing, China. [4]Central Analytical Research Facility, Institute for Future Environments, Queensland University of Technology, Brisbane, QLD, Australia. [5]School of Mechanical, Medical and Process Engineering, Queensland University of Technology, Brisbane, QLD, Australia. ✉e-mail: xiaolei.shi@qut.edu.au; zhigang.chen@qut.edu.au

different wavelengths to encounter more obstacles during propagation and subsequently undergo scattering, thereby reducing the κ_l. However, these defects may also scatter charge carriers, thereby reducing the carrier mobility μ and lowering the σ, which makes the optimization of thermoelectric performance a challenging task.

Wearable thermoelectric devices operate based on the temperature different (ΔT) between the body surface and the surrounding environment[7]. Therefore, the materials in these devices need to exhibit high thermoelectric performance and flexibility within the near-room temperature range[2]. Bi_2Te_3 has been widely regarded as one of the best thermoelectric materials for near-room temperature applications[8]. However, limitations such as high costs and inherent brittleness hinder the assembly of flexible films using Bi_2Te_3-based materials[7,9,10], making practical wearable applications challenging. As alternatives, silver chalcogenides Ag_2X (where X is S, Se, and Te) show promising potential for near-room temperature applications[11]. Compared to Bi_2Te_3, Ag_2S exhibits good ductility but lower thermoelectric performance[12]. Ag_2Te is more brittle and has relatively high intrinsic n, resulting in insufficient thermoelectric performance optimization[13]. In this context, Ag_2Se, after certain optimizations, can exhibit good thermoelectric performance in the near-room temperature range and can exhibit greatly improved ductility through doping, compositing, and hybridization strategies[14–16]. Currently, methods for preparing Ag_2Se films include vacuum filtration[17,18], cation exchange[19], screen-printing[20], co-evaporation[21], magnetron sputtering[22,23], and physical-vapor-deposition (PVD) methods[24]. As of today, the reported $S^2\sigma$ of Ag_2Se-based films has sharply increased from 8 to 27 μW cm^{-1} K^{-2} [17–22,24–26]. Given its remarkable development pace, the potential application of Ag_2Se in wearable/portable devices is evident.

Despite the flourishing research on Ag_2Se films, significant controversies persist within this material system[14]. A major point of contention revolves around the relationship between the orientation of Ag_2Se films and their thermoelectric performance. For example, compared to (013)-textured films, the films with strong (00 l) can yield high S and a high $S^2\sigma$ of 21.6 μW cm^{-1} K^{-2} [27]. This enhancement can be achieved in the oriented films by adjusting the Ag to Se ratio[27]. However, stronger (00 l) oriented Ag_2Se films show significantly lower σ compared to those that are (013) oriented[17]. Other works reported that a strongly (201)-oriented Ag_2Se thin film, prepared by PVD, exhibited a $S^2\sigma$ of 25.9 μW cm^{-1} K^{-2} within the near-room temperature range[24]. More recently, Te-doping-triggered strong (00 l)-oriented Ag_2Se films, prepared by co-evaporation, showed a $S^2\sigma$ exceeding 24.8 μW cm^{-1} K^{-2} [28]. However, these studies, focusing on film preferred orientation, are still lacking clear experimental and theoretical validations[14]. Furthermore, most of these studies have not clarified the relationship between the preferred orientation observed through X-ray diffraction (XRD) and the orientation during performance measurement, as the direction of thermoelectric performance testing is typically in-plane, while XRD observation of film orientation is usually conducted in the out-of-plane direction. Therefore, those discussions regarding the thermoelectric performance of Ag_2Se based on crystal orientation remain contentious[14]. Additionally, many previously reported strategies for enhancing the thermoelectric performance of Ag_2Se thin films have focused on increasing σ, often targeting values above 2000 S cm^{-1} to achieve a higher $S^2\sigma$[29]. However, a major drawback of this approach is that high σ also increases the κ_e of the film, a fact that is often overlooked. Therefore, effectively enhancing the S of Ag_2Se thin films to improve overall thermoelectric performance should be the primary focus of research. Furthermore, there is still room for improving the practical application potential of the Ag_2Se films, such as further improving their thermoelectric performance and stability, as well as simplifying the fabrication process[14].

In this study, guided by the first-principles density functional theory (DFT) calculations and by finely adjusting the parameters of the selenization reaction, the orientation of Ag_2Se thin films can be favorably altered, leading to high μ (~1500 cm^2 V^{-1} s^{-1}) and σ (1387 S cm^{-1}), and in turn, an $S^2\sigma$ of 30.8 μW cm^{-1} K^{-2} at 343 K, which ranks as a top value in the literature[17,24,25,27,28,30–33]. Through computational calculations and characterizations, the presence of slight Se vacancies (V_{Se}) and elemental Ag nanoinclusions in the thin films can be found to contribute to this exceptional thermoelectric performance. Furthermore, by introducing ethanol to reduce the liquid surface tension of the Se precursor, the adhesion of Ag_2Se thin films to the polyimide (PI) substrate can be improved, ensuring the overall flexibility and durability of the films. Building upon this improvement, a slotted thermoelectric device was assembled. At a temperature difference (ΔT) of 20 K, the device generated a maximum output power (P) of 0.58 μW, a power density (ω) of 807 μW cm^{-2}, and a normalized power density (ω_n) of 1.8 μW cm^{-2} K^{-2}.

Results and discussion

Although there is currently considerable debate surrounding the preferred orientation of Ag_2Se thin films, there are still certain pivotal criteria that can be followed. For example, it is crucial to identify suitable crystal orientations that can enhance the weighted mobility (μ_w), thereby increasing the $S^2\sigma$ (quality factor). Consequently, we followed the guideline of seeking higher μ to design Ag_2Se thin films with optimal orientations. To achieve this objective, we first investigated the crystal structure of Ag_2Se. As depicted in Fig. 1a, near-room-temperature Ag_2Se features an orthorhombic structure (powder diffraction file PDF#010807685)[34]. Within the crystal structure, silver ions (Ag^+) and selenium ions (Se^{2-}) are arranged in the lattice in specific proportions. Consequently, the arrangement of Ag and Se atoms varies across different crystal planes. Figure 1b illustrates the calculated electron charge density distributions on the nearly parallel planes, specifically (002), (013), and (014). Here, "nearly parallel planes" indicates that (013) and (014) form a small angle (<15°) with (002), with only a 4° angle between (013) and (014). Supplementary Figs. 1 and 2 display the charge density distributions on planes perpendicular to (00 l) and (01 l). In comparison to the views of (100) and (010) planes with high charge accumulation, the (00 l) plane exhibits relatively ordered periodic and lower charge concentration[17]. High charge density distribution may trap the carriers, and prevent electrons gaining sufficient energy for transition, reducing the effective carrier concentration during thermoelectric testing. It should be noted that the observed out-of-plane (00 l) in XRD indicates that the thermoelectric performance test is conducted along the in-plane direction, which is perpendicular to the (00 l) plane. Similarly, the (01 l)-perpendicular planes show a non-uniform charge distribution with a larger periodic structure. This uneven distribution causes electron-electron and electron-atom collisions during transit, resulting in unnecessary carrier scattering and a subsequent decrease in μ. In contrast, planes like (h00)/(0k0), which are perpendicular to (01 l)/(00 l), exhibit a more uniform distribution, offering potential for higher μ. Therefore, to achieve Ag_2Se thin films with enhanced μ, we focus on orientations perpendicular to the nearly parallel (00 l) planes.

In a thermoelectric thin film, the measured thermoelectric property is in-plane direction while the XRD scanning direction is out-of-plane of thin film, as depicted in Fig. 1c (bottom). This implies that when the obtained XRD patterns of the thin film show a strong nearly parallel planes of (00 l), it is possible for the strong anisotropy along the direction of thermoelectric performance measurement to be (100), (010) or other planes perpendicular to nearly parallel planes of (00 l). In other words, when the thin film shows strong nearly parallel planes of (00 l)-oriented, the measured macroscopic in-plane μ and σ will be higher. Therefore, it is better to obtain nearly parallel planes of (00 l)-oriented Ag_2Se thin films, suggested by XRD.

In contrast to the previous reports, such as Te-doping-triggered orientation adjustment[28], our objective is to design a relatively simple synthesis method that avoids unnecessary orientations while

https://doi.org/10.1038/s41467-025-56671-7

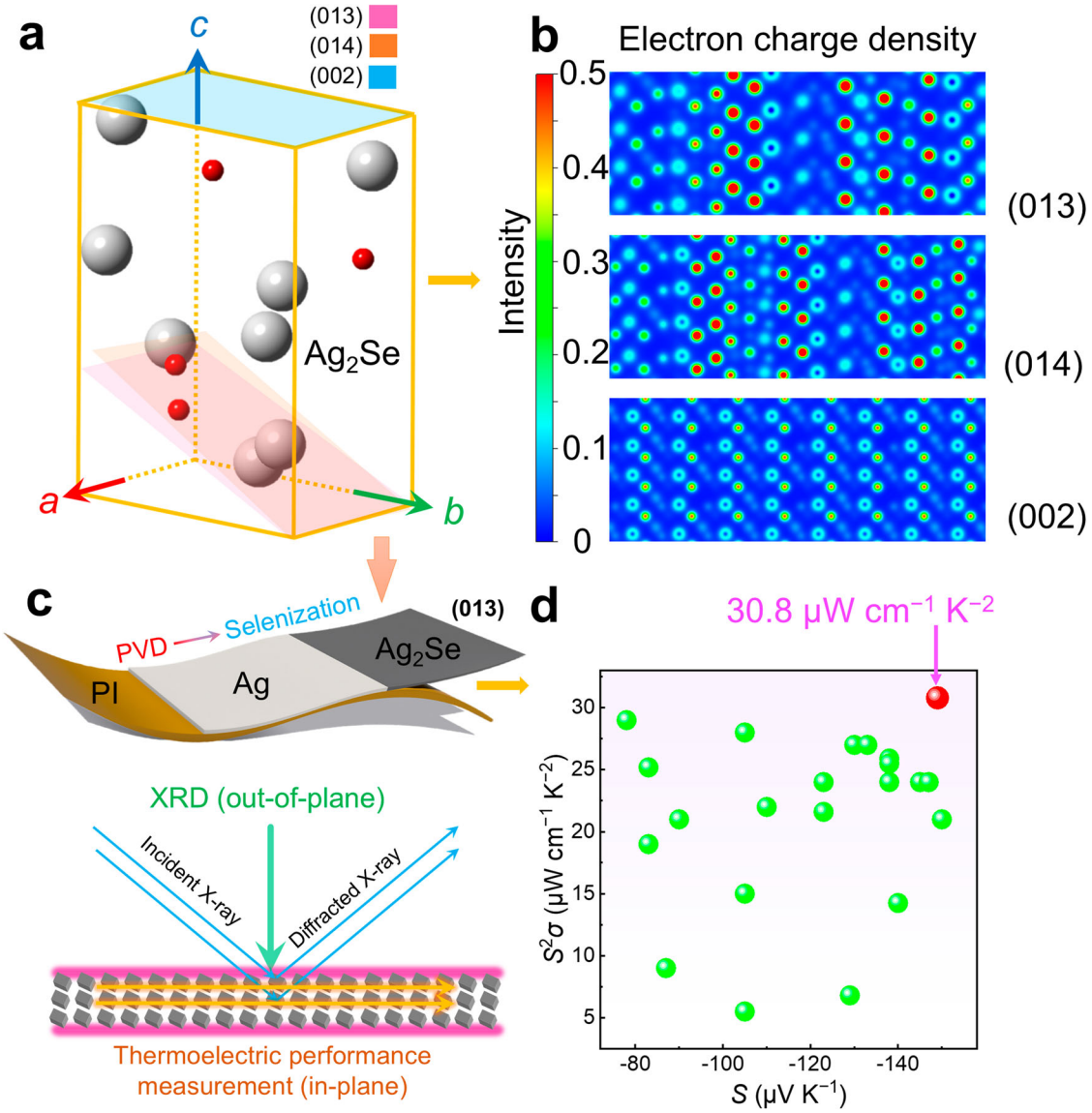

Fig. 1 | Introduction of highly orientated Ag_2Se thin films. a Unit cell of orthorhombic Ag_2Se (powder diffraction file PDF#010807685) with highlighted (013), (014) and (002) planes. **b** Electron charge density distribution for the nearly parallel planes (013), (014) and (002). **c** Illustrations of the fabrication process of the Ag_2Se thin film and the comparison of the directions between the X-ray diffraction (XRD) detection and thermoelectric performance measurement. **d** Comparison of maximum power factor ($S^2\sigma$) between this work and reported Ag_2Se thin films in recent years[17,24,25,27,28,30–33,36–46].

quantitatively demonstrating its application potential. With these goals, we proposed a combined approach using electron beam deposition and solution immersion to prepare Ag_2Se thin films, as illustrated in Fig. 1c (top). More detailed fabrication processing and reaction principles is illustrated in chemical reaction principles and Supplementary Fig. 3 in the Supporting Information. The two-step fabrication method promotes the preferred orientation in Ag_2Se thin films. To rigorously analyze the film orientation, we utilized two XRD scan modes. The 2θ scan (grazing incidence X-ray diffraction (GIXRD) scan modes) provides a broad view of crystallographic orientations in the sample, helping to identify the presence of any texture or preferred orientation. However, due to the limitations of the 2θ geometry, it may not reveal the specific planes with preferential alignment. In contrast, the symmetric θ-2θ scan emphasizes diffraction peaks associated with dominant texture features, enhancing preferred orientations while potentially suppressing other planes. This makes the θ-2θ scan particularly effective for identifying primary texture characteristics, albeit with reduced sensitivity to less prominent orientations. First, Ag thin films with a specific (111) preferred orientation were deposited on PI substrates using electron beam deposition, as shown in Supplementary Figs. 4 and 5. The (111) orientation of Ag, recognized for its close-packed spherical arrangement, demonstrates excellent adsorption with chalcogenides, which facilitates a thorough reaction with the Se precursor. This results in pre-heat-treatment samples with anisotropic properties, as shown in Supplementary Figs. 6 and 7[35]. Please note that the Al peak in Supplementary Fig. 7 originates from the XRD holder and is not from the sample itself. Subsequently, through manipulation of thermal treatment, preferred orientation of (002), (013), and (014) were achieved. The significant orientation change may result from the recrystallization process occurring during heat treatment at 180 °C. With this strategy, we achieve an exceptionally high $S^2\sigma$ value of 30.8 μW cm^{-1} K^{-2}, exceeding previously reported values, as shown in Fig. 1d[17,24,25,27,28,30–33,36–46], Supplementary Fig. 8[17,18,21,24,25,27,28,30–33,37–40,47–56], and Supplementary Table 1[15,17,18,20,24,26–28,30,32,37,47–50,52–67] in the Supporting Information. From the comparation, it should be noted that our $S^2\sigma$ is mainly contributed by S, which offers potential for achieving thin-

https://doi.org/10.1038/s41467-025-56671-7

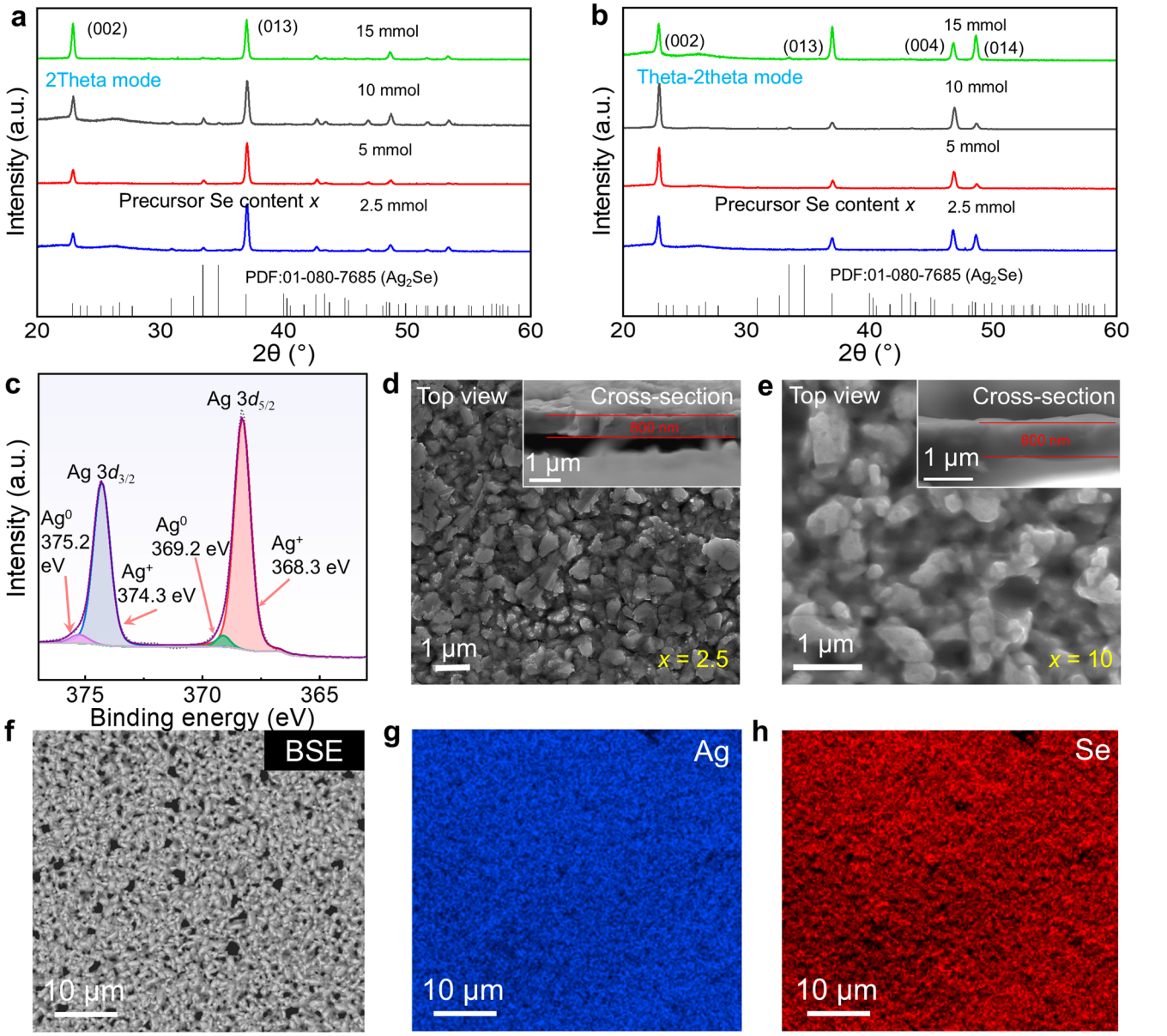

Fig. 2 | Phase, structures, and compositions of Ag_2Se thin films. a Grazing incidence diffraction GIXRD patterns (2θ mode) of Ag_2Se thin films prepared at different Se precursor contents x ($x = 15$, 10, 5, and 2.5 mol). The 2θ ranges from 20° to 60°. **b** Symmetric mode (θ–2θ mode) of Ag_2Se thin films prepared at different Se precursor contents x ($x = 15$, 10, 5, and 2.5 mol). The 2θ ranges from 20° to 60°. **c** X-ray photoelectron spectroscopy (XPS) spectra of Ag $3d_{3/2}$ and Ag $3d_{5/2}$ for the thin film with $x = 10$ mmol. Scanning electron microscopy (SEM) images of thin films with **d** $x = 2.5$ mmol and **e** $x = 10$ mmol from top views. The insets show corresponding SEM images from cross-sectional views. **f** SEM backscattered electron (BSE) image along with corresponding energy dispersive X-ray spectroscopy (EDS) maps of **g** Ag and **h** Se in the film with $x = 10$ mmol.

film device application, as higher S leads to an increased output voltage (V_{oc}).

To elucidate the influence of Se precursor on the macroscopic orientation of Ag_2Se films, we varied the precursor concentration (x) during the selenization process, with $x = 15$, 10, 5, 2.5, and 1.25 mmol, for investigation and measured their GIXRD pattern, Fig. 2a is a 2θ mode pattern, displaying the lattice information of Ag_2Se thin films in the 2θ range of 20 to 60°. All diffraction peaks match well with the standard near-room-temperature Ag_2Se PDF card (#010807685), and no apparent impurities can be detected within the precision range of XRD examination. A rightward peak shift can be observed (Supplementary Figs. 9 and 10), possibly attributed to lattice contraction, caused by spontaneous selenium vacancies (V_{Se}) in the films. As shown in Fig. 2a (2theta mode pattern), Ag_2Se thin films prepared from different concentration precursors exhibit preferred orientation existing, which might be (002) and (013). However, as mentioned above, 2θ mode is not precise enough to judge the position of preferred orientation. Therefore, as shown in Fig. 2b, the XRD symmetric θ-2θ mode pattern reveals that the thin film exhibits preferred orientations along three main textures: (00 l), (013), and (014). These orientations can be considered nearly parallel planes relative to (00 l). The Lotgering factor of (00 l), (013), and (014) can be seen in Supplementary Fig. 11.

According to Fig. 2b, when $x = 2.5$, 5 and 10 mmol, Ag_2Se films show a strong (002) orientation. When $x = 15$ mmol, the (013)/ (014) orientation begins to strengthen. For the sample with $x = 1.25$ mmol, its uniqueness lies in the distinct presence of pure Ag peaks alongside the monoclinic crystal phase of Ag_2Se in the diffraction pattern, attributed to an excess of Ag due to insufficient Se sources during the selenization reaction, as shown in Supplementary Fig. 12. Moreover, when the Se concentration is too low, there is a competition reaction between S

and Se in the precursor during selenization (the precursor includes $Na_2S{\cdot}9H_2O$ and Se powder). Due to the much lower concentration of Se atoms compared to S atoms, a transition phase of $Ag_2Se_\delta S_{1-\delta}$ is formed[68], as shown in Supplementary Fig. 13. Specifically, the samples with $x = 2.5$, 5, and 10 mmol exhibit similar preferential orientations, predominantly along the (00 *l*) planes, with noticeable (013)/(014) orientations also present. Since no additional elements were introduced into the system and the heat treatment conditions remained consistent, we attribute the formation of these nearly parallel (00 *l*) planes to the recrystallization of the films during the heat treatment process. In contrast, the $x = 15$ mmol sample displays a stronger (013)/(014) orientation. This difference can be attributed to the fact that, as shown in Supplementary Figs. 9 and 10, its unit cell contraction is less pronounced compared to the other samples. This suggests that it may have fewer Se vacancies, potentially leading to more distinct (013)/(014) orientations during the recrystallization process.

To investigate the extent of residual elemental Ag in the films after solution-phase selenization, we examined the valence state of Ag in the films at $x = 10$ mmol by X-ray photoelectron spectroscopy (XPS). As shown in Fig. 2c, the XPS spectrum primarily displays Ag^+ valence states associated with the Ag_2Se matrix with a small amount of Ag^0, and the peak positions are consistent with values reported in the literature[69,70]. However, at $x = 10$ mmol, we did not observe crystalline signals of pure Ag in the GIXRD diffraction pattern. One potential reason may be due to the extremely small amount of residual crystalline Ag that is below the detection limit of XRD when the Se precursor concentration is sufficiently large, while another reason should be that the sample at $x \geq 2.5$ mmol may contain a small amount of nano-crystalline Ag, which is difficult to be examined by XRD due to its board humps.

To better understand the structure and composition of Ag_2Se films prepared from solutions with different concentrations of Se precursor, we investigated sample morphology using scanning electron microscopy (SEM) and conducted energy-dispersive X-ray spectroscopy (EDS) analysis to analyze composition. Figures 2d and 2e display top-view SEM images of Ag_2Se films with $x = 2.5$ and 10 mmol, revealing significant differences in morphology. This observation reinforces the notion that, despite the similar preferred orientations indicated by the XRD results, variations in precursor concentration still influence the morphology and crystallization of the thin films. Consequently, these differences in morphology can potentially lead to variations in the performance of the thin films. Insets in Fig. 2d, e show cross-sectional SEM images, indicating an average film thickness of approximately 800 nm. To investigate the uniformity of film composition, the backscattered electron (BSE) image and corresponding EDS maps of the sample with $x = 10$ mmol are provided in Fig. 2f–h. As can be seen, the distributions of Ag and Se are uniform without significant elemental segregation. Additional SEM and corresponding EDS information on samples prepared using different Se precursor contents are shown in Supplementary Figs. 14–24 in the Supporting Information.

To obtain insights into the microstructure and detailed composition of Ag_2Se thin film, we prepared transmission electron microscopy (TEM) specimens using focused ion beam (FIB) technology for characterization using aberration-corrected scanning TEM (Cs-STEM). Figure 3a depicts a low-magnification high-angle annular dark-field (HAADF) image of the FIB-prepared sample of Ag_2Se film with $x = 10$ mmol. The image reveals a relatively dense film without significant porosity, exhibiting good continuity at the microscopic scale. However, some defect-like structures causing local variations in image contrast are observed. Additionally, insets depict corresponding selected-area electron diffraction (SAED) patterns, confirming the view direction of the FIB sample along [100]. Since the observation plane of the samples prepared by FIB is perpendicular to the film (owing to the FIB preparation method), this confirms a high probability of subsequent film thermoelectric performance measurement along [100] (parallel to the (100) orientation), aligning with our experimental design concept. Figure 3b is a high-resolution Cs-STEM HAADF image from a normal area selected from Fig. 3a. The lattice arrangement in the selected area appears ordered, confirming that the normal matrix of the film is highly crystalline, validating our film preparation process to achieve high crystalline quality. The viewed zone axis is along the [100] direction, indexed by the corresponding unit cell shown in Supplementary Fig. 25 for reference. However, the image presents lattice distortion along a certain direction. Figure 3c, obtained from an area near the contrast difference in Fig. 3a, highlights potential point defect regions within the matrix, likely originating from V_{Se}, which aligns with the rightward peak shift observed in the XRD results. Figure 3d presents a Cs-STEM HAADF image from a typical area selected from Fig. 3a, accompanied by corresponding strain maps in different directions, which reveal significant strain in the *x*-direction, indicating potential lattice distortion. Figure 3e, from another region near the defect, exhibits a stronger contrast difference, indicating more pronounced lattice distortion. The inset shows the corresponding fast Fourier transform (FFT) pattern. Its slight pattern overlap confirms subtle variations in the zone axis due to severe lattice distortion in that area. Figure 3f provides a filtered image corresponding to Fig. 3e, exhibiting a typical interplanar spacing of 3.81 Å in the (002) orientation, perpendicular to the [100], which can be corroborated with the previous XRD results, and potential edge-like dislocations within the selected range (marked by red squares). The inset image shows an enlarged view of the red square-marked area, featuring a suspected edge-like dislocation possibly triggered by the formation of V_{Se}. Figure 3g is an enlarged image of the highly distorted area in Fig. 3a, revealing ripple-like lattice contrast differences, indicating more pronounced lattice distortion, supported by the observed overlapping FFT pattern shown in Fig. 3h as inset. Figure 3i displays a low-magnification Cs-STEM HAADF image, corresponding EDS maps, and determined atomic ratios of Ag and Se. Overall, the distribution of elements appears relatively uniform, but slight Ag enrichment regions can be observed from the EDS and HAADF images (as indicated by arrows). Combining the micro-area EDS results from Fig. 3i with our previous XRD and XPS results, we infer the presence of minor amorphous pure Ag inclusions in the sample. For comprehensive lattice calibration information, refer to the SAED images in Supplementary Fig. 26.

To illustrate the potential impact of V_{Se} and elemental Ag formation on the thermoelectric properties of Ag_2Se thin films, we conducted first-principles calculations using DFT. Initially, we computed the formation energies of Ag vacancies (V_{Ag}), V_{Se}, and point defects by Se replacing Ag (Se_{Ag}), which were found to be 2.57, 1.15, and 5.07 eV, respectively. The formation energy of V_{Se} at only 1.15 eV suggests their likelihood to exist during the solution-phase selenization process of Ag films, leading to lattice contraction, consistent with the overall right shift observed in XRD characteristic peaks. Consequently, the actual film should exhibit n-type semiconductor transport characteristics. Furthermore, we calculated the band structures of intrinsic Ag_2Se and Ag_2Se with Ag and Se vacancies, as well as the band structure of pure Ag. Figure 4a illustrates the band structure of intrinsic Ag_2Se, where it is evident that the semiconductor properties of pristine Ag_2Se are contributed by both the valence band and conduction band. Figure 4b depicts an enlarged view of the Fermi level position in the band structure of intrinsic Ag_2Se. The conduction band is seen to intersect the Fermi level, suggesting that the material may exhibit semi-metallic characteristics. However, theoretical calculations are generally performed under 0 K conditions, which can introduce discrepancies compared to experimental results. Consequently, we speculate that pristine Ag_2Se may have an extremely narrow bandgap, allowing for higher excitation energies of electrons that facilitate electron transitions. This characteristic could significantly contribute to its high σ. In the presence of V_{Ag} (Fig. 4c), higher contributions from the valence

https://doi.org/10.1038/s41467-025-56671-7

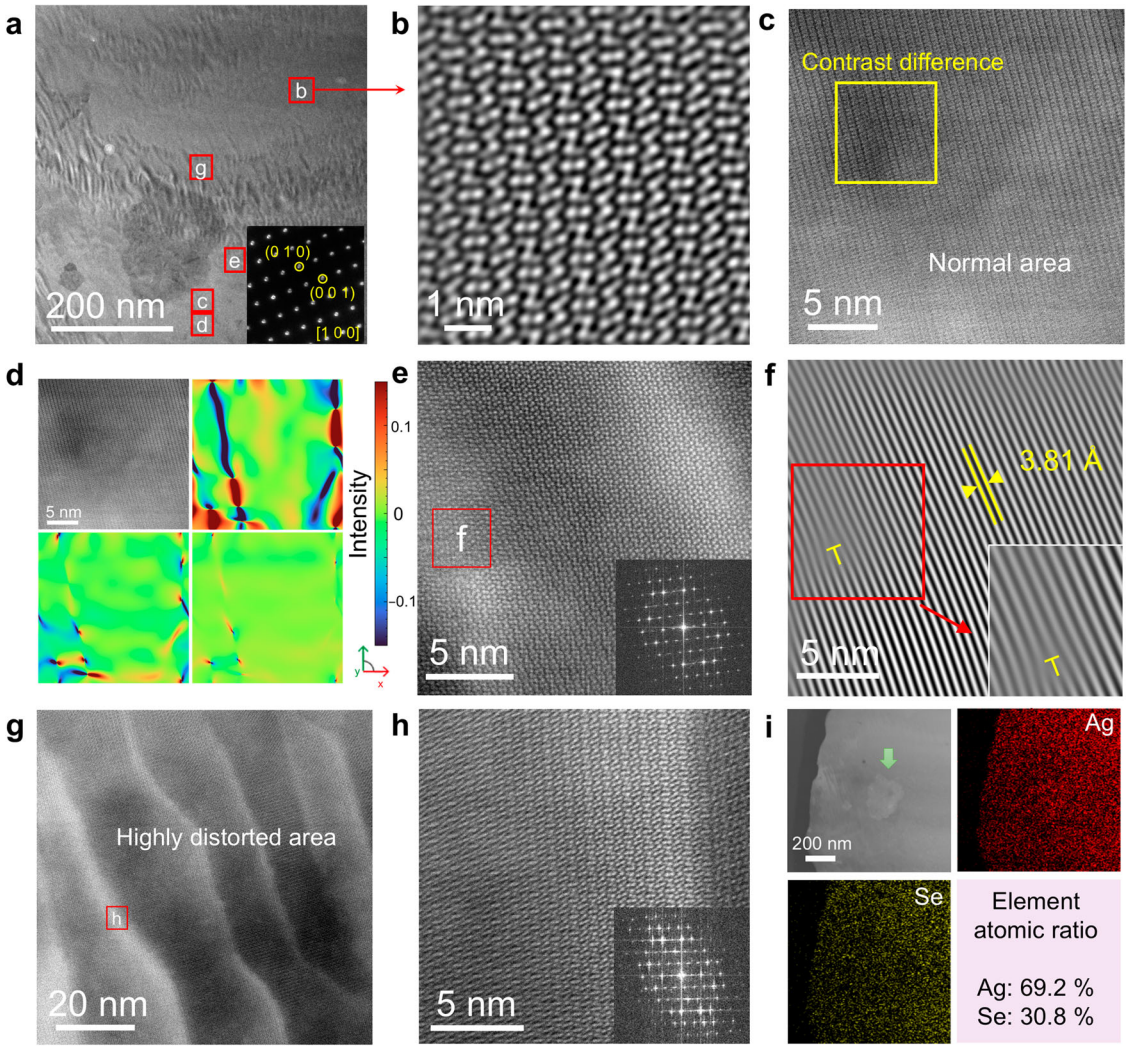

Fig. 3 | Micro/nanostructural characterizations of Ag_2Se thin film with $x = 10$ mmol. a Transmission electron microscopy (TEM) high-angle annular dark-field (HAADF) image of the specimen prepared by focused ion beam (FIB) technique. The inset is the corresponding selected area electron diffraction (SAED) pattern with indexed lattice information. **b** High-resolution spherical aberration-corrected scanning TEM (Cs-STEM) HAADF image of the matrix taken from a normal area in (**a**). **c** Cs-STEM HAADF image with areas of different contrast caused by intensive point defects taken from (**a**). **d** Cs-STEM HAADF image with corresponding strain maps along different directions. **e** Another Cs-STEM HAADF image taken from (**a**). The inset is the corresponding fast Fourier transform (FFT) pattern with indexed lattice information. **f** Filtered image taken from e suggesting the potential presence of edge-like dislocation. The inset shows the magnified edge-like dislocation area. **g** Cs-STEM HAADF image taken from the highly distorted area in (**a**). **h** Cs-STEM HAADF image taken from (**g**) with highly distorted area. The inset shows the corresponding FFT pattern with indexed lattice information. **i** HAADF image of a particle in the matrix of Ag_2Se with corresponding EDS maps and determined atomic ratio between Ag and Se.

band lead to a material transition towards p-type conductivity. This transition is further evidenced by the enlarged electronic structure (Fig. 4d). However, as mentioned earlier, the formation of V_{Ag} in Ag_2Se is challenging, which is why practical Ag_2Se materials exhibit n-type thermoelectric properties. Conversely, in the presence of V_{Se}, the conduction band crosses the Fermi level, with the conduction band contributions prominent in the band structure, resulting in typical n-type thermoelectric characteristics of the material, as shown in Fig. 4e. Figure 4f illustrates the band structure of pure Ag, where conduction and valence bands overlap, exhibiting typical metal conductivity. However, the significant electronic structural differences between Ag and Ag_2Se may lead to the presence of Ag nanoscale inclusions in the Ag_2Se samples potentially enhancing both κ_l and S.

To determine the specific impact of precursor Se content on the thermoelectric properties of Ag_2Se thin films, we measured the thermoelectric properties of Ag_2Se films corresponding to $x = 15, 10, 5$, and 2.5 mmol. The performance of the sample with $x = 1.25$ mmol can be found in Supplementary Fig. 27, where severe inadequacy in selenization significantly affects the overall thermoelectric properties of the film due to the decisive influence of Ag on the thermoelectric properties. Figure 5a–c display the temperature-dependent σ, S, and $S^2\sigma$ of Ag_2Se. As can be seen, Ag_2Se films with $x = 10$ and 5 mmol exhibit higher σ, leading to $S^2\sigma$ values as high as 30.8 and 27.5 μW cm^{-1} K^{-2} at 343 K, respectively. The result of $S^2\sigma > 30$ μW cm^{-1} K^{-2} can be repeated when the material was synthesized by selenization process with a selenium precursor at $x = 10$ mmol under E-beam deposition conditions with voltages (V) and currents (I) of 10 kV and 31 mA, respectively, which are depicted in Supplementary Figs. 28 and 29. The measurement method using ZEM-3 is illustrated in Supplementary Fig. 30. When the x is sufficiently large (x greater than or equal to 5 mmol), the S are essentially the same, indicating that the change in thin-film orientation has a weak effect on the S, as hypothesized earlier. When x is small (such as $x = 2.5$ mmol), the presence of more residual Ag impurities significantly reduces the S. Compared with other

https://doi.org/10.1038/s41467-025-56671-7

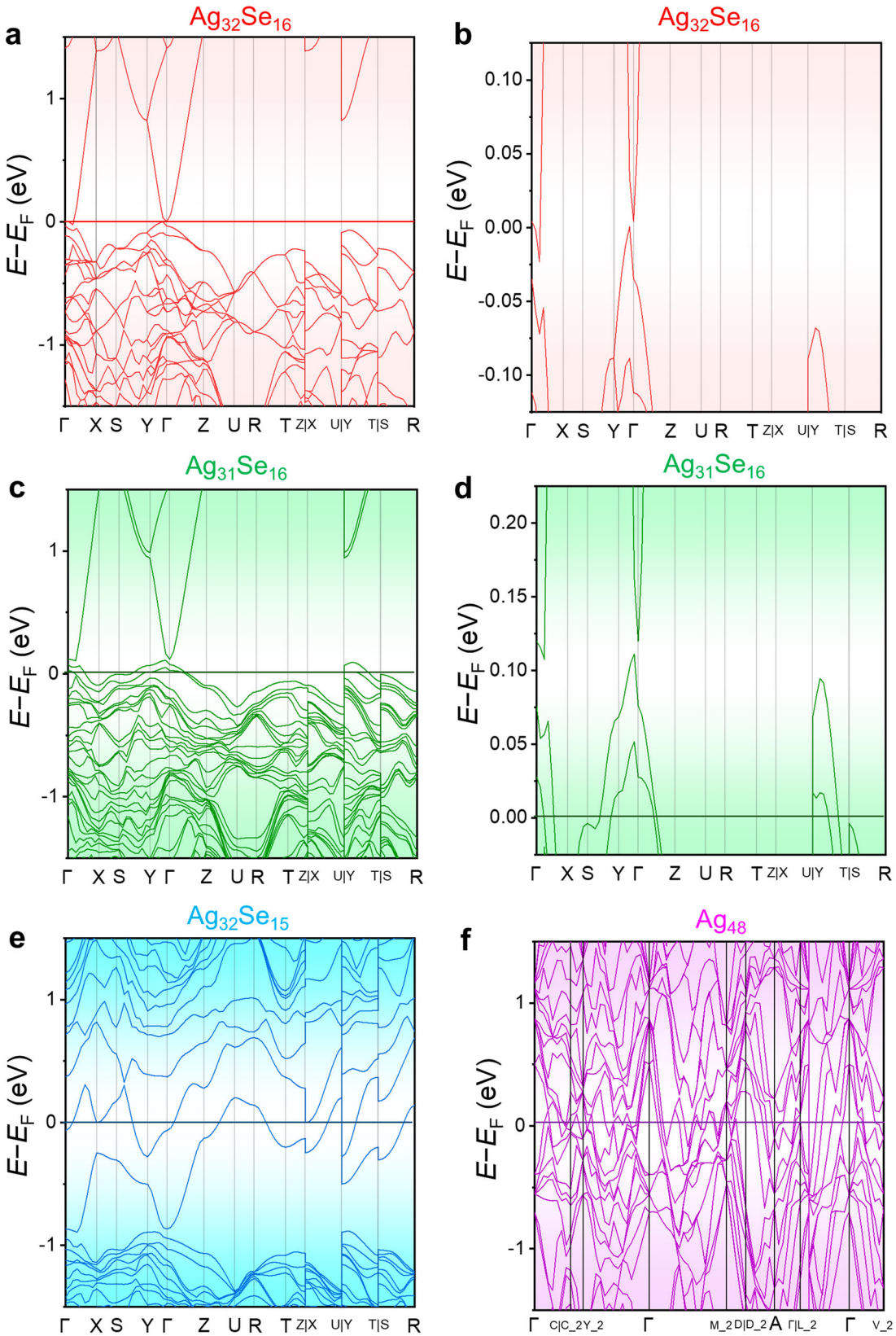

Fig. 4 | Electronic structures of $Ag_2Se_{1-\delta}$/Ag. Calculated band structures of **a** pristine Ag_2Se ($Ag_{32}Se_{16}$), **b** magnified $Ag_{32}Se_{16}$, **c** Ag_2Se with Ag vacancies ($Ag_{31}Se_{16}$), **d**, magnified $Ag_{31}Se_{16}$, **e** Ag_2Se with Se vacancies ($Ag_{32}Se_{15}$), and **f** pure Ag (Ag_{48}).

literature[17,24,25,27,28,30–33,36–46], our as-fabricated thin-film sample with precursor Se content $x = 10$ mmol exhibit relatively good value in both σ and S, which results in overall optimized $S^2\sigma$. This phenomenon may be attributed to the energy filtering effect[71].

To explore deeper into the nature of the variations in σ and S, we explored the relationship between μ and n at room temperature for different films, as shown in Fig. 5d. Ag_2Se films with $x = 10$ and 5 mmol exhibit high μ values of 1500 $cm^2 V^{-1} s^{-1}$, validating the correctness of

https://doi.org/10.1038/s41467-025-56671-7

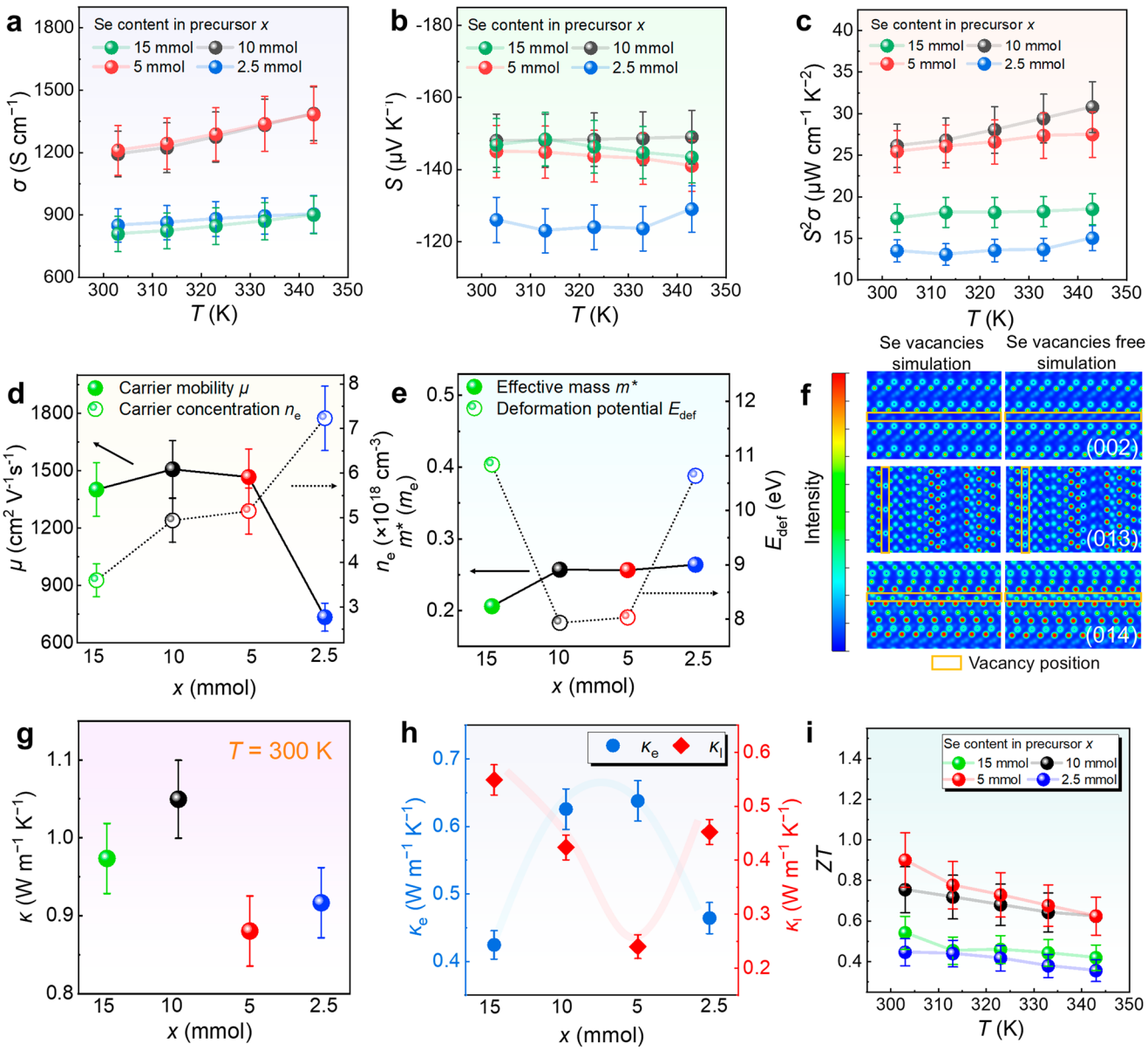

Fig. 5 | Thermoelectric performance and charge distribution of Ag_2Se thin films at different Se precursor content x (x = 15, 10, 5, 2.5 mmol). Temperature-dependent **a** electrical conductivity (σ), **b** Seebeck coefficient (S), and **c** $S^2\sigma$. Here, 5% error bars are employed. **d** Room-temperature carrier concentration (n) and mobility (μ) as a function of x. Here, 5% error bar is employed **e** Room-temperature effective mass (m^*) and deformation potential (E_{def}) as a function of x calculated by a single parabolic band (SPB) model. **f** Comparison of the charge distribution maps for Ag_2Se with Se vacancies along different orientations. x-dependent room-temperature **g** thermal conductivity (κ) and **h** lattice thermal conductivity (κ_l) and electrical thermal conductivity (κ_e). Here 10% error bar is employed for (**g**), and 5% error bar is employed for (**h**). **i** Estimated temperature-dependent ZT. Here 5% error bar is employed.

our orientation design concept. Additionally, the values of n fall within the range of 4.94×10^{18} cm^{-3}, which is within a reasonable range compared to the reported optimal n of $1–2 \times 10^{18}$ cm^{-3} [68]. In this regard, the n of Ag_2Se films synthesized under x = 15 mmol precursor is closer to the optimal n. Moreover, the μ of the samples with x = 10 mmol and 5 mmol is similar. However, the overall electrical performance of the x = 15 mmol sample is lower. This can be explained by thin film anisotropy. Considering the XRD analysis results provided earlier, Ag_2Se films prepared with x = 10 and 5 mmol exhibit a stronger preferred orientation along the (00 l) direction, where the in-plane direction (i.e., the direction of properties testing) results from planes perpendicular to nearly parallel planes of (00 l) and (01 l) such as (100) and (010), thus facilitating excellent charge transport. However, samples with precursor x = 15 mmol exhibit strong orientation in (002), (013), and (014) directions, complicating the crystal orientation for in-plane performance testing. This complexity might lead to significant carrier scattering at grain boundaries during the transport, resulting in a decrease in overall conductivity. For Ag_2Se films synthesized with precursor concentration x = 2.5 mmol, the relatively pronounced unit cell contraction observed in the GIXRD results, combined with the increased in-plane nanoinclusions resulting from the lower precursor concentration, leads to higher n and lower μ. This combination ultimately results in a simultaneous degradation of both the S and σ.

To explain the variation in n and μ of the thin films, the effective mass m^* and deformation potential E_{def} of films with different x at room temperature were calculated by using the single parabolic band (SPB) model[72], as shown in Fig. 5e. The variation in m^* is not particularly significant, mainly due to the insignificant change in n with varying precursor concentration x. For the sample with x = 15 mmol, the change in m^* might stem from the lower n value. Additionally, with

decreasing x, a slight increase in m^* can be seen, attributed to the reduced completion degree of the selenization reaction, implying more residual nanoscale Ag inclusion phases. Since more residual inclusion phases increase the average intensity of interfaces between the nanophase and the Ag_2Se matrix, the energy filtering effect becomes more pronounced, thus leading to more scattering of low-energy carriers and in turn, an increase in m^*. Ag_2Se films synthesized with precursor concentrations $x = 10$ and 5 mmol exhibit relatively low E_{def}, indicating relatively easy lattice deformation capabilities. This indirectly confirms the enhanced orientation of the films, leading to relatively higher μ. Therefore, we demonstrate the consistency between the experimental and calculated results of the electrical transport properties.

Furthermore, considering the presence of V_{Se} in actual thin-film materials, we calculated the charge distribution of Ag_2Se incorporating V_{Se}, as shown in Fig. 5f. Compared to the (002), (013), and (014) planes in Ag_2Se without V_{Se}, clear atomic vacancies are observed in the charge distribution of Ag_2Se with V_{Se}, resulting in a more uneven charge density distribution. Consequently, from the calculated charge distribution results, we can infer the significance of achieving a strong orientation.

Besides the electrical transport properties of the thin-film materials, we utilized the laser photothermal intensity technique (PIT) alternating current (AC) method for thermal diffusivity D measurements. The methodology and principles for testing D of thin films are described in Supplementary Figs. 31 to 35. To calibrate the κ of the films, we determined the Lorentz parameters L of Ag_2Se films by the SPB model (refer to Supplementary Fig. 36) and calibrated the porosity (refer to Supplementary Fig. 37). Porosity is inversely proportional to material density (ρ); therefore, as porosity increases, the material density decreases. Since the results obtained from the equipment are thermal diffusivity (D), and according to the formula $D = \frac{\kappa}{\rho c}$ (here c refers to specific heat capacity), the ρ directly affects the calculation of κ. Therefore, we used ImageJ software to calibrate porosity, aiming to obtain relatively accurate values of κ. In this context, we obtained convincible κ data for Ag_2Se films, as shown in Fig. 5g. Overall, the κ of the films are relatively low. Figure 5h compares the κ_e and κ_l of the Ag_2Se films. κ_e can be calculated using the formula $\kappa_e = L\sigma T$[73], and κ_l can be calculated by subtracting κ_e from κ. It can be observed that for Ag_2Se film samples with $x = 10$ and 5 mmol, the κ_l are relatively low due to the presence of defects in various dimensions observed in TEM characterizations. However, the κ_e are relatively high, which is mainly attributed to the excellent σ. Based on reliable measurements of σ, S, and κ, we obtained the overall room-temperature ZT for Ag_2Se films with different x, reaching a maximum value of 0.9, as shown in Fig. 5i. Theoretical and experimental ZT as a function of n calculated from the SPB model are presented in Supplementary Fig. 38 for reference.

To quantify the practicality of the films, we conducted durability and flexibility tests on Ag_2Se films. Figure 6a displays the performance changes of the films before and after exposure to the air for six months. There is no significant performance change, demonstrating that Ag_2Se films prepared using electron beam and solution methods exhibit high stability. The slight increase in $S^2\sigma$ may be attributed to the effect of humidity on S[74]. This high longevity may stem from the well-crystallized nature of the thin films. Furthermore, we subjected samples prepared with different x to 1000 cycles of bending with a r of 5 mm (Fig. 6b and Supplementary Fig. 39), as well as 200 cycles of bending for the Ag_2Se thin film with $x = 10$ mmol at different r values (Fig. 6c). The inset in Fig. 6c illustrates the process and method of the bending test. The results indicate that the normalized resistance change ($\Delta R/R_0$) of the film consistently stays within 10%, reflecting the high stability and flexibility of Ag_2Se films. The high flexibility and stability are derived from the optimized processes of electron beam evaporation and subsequent selenization reactions, controlling the thickness of the film, and ensuring excellent contact between the film and the flexible PI substrate.

To validate the practical application potential of the prepared thin film, we designed a novel slotted thin-film device, as illustrated in Fig. 6d (with dimensions detailed in Supplementary Fig. 40). The device consists of three sets of three-leg modules connected in series. This configuration enables the stacking of multiple modules to achieve high-performance output. As shown in Fig. 6e, f, under a ΔT of 20 K, the V_{oc} can reach up to 27.1 mV, and the output power (P) reaches 0.58 μW. The power density (ω), as depicted in Fig. 6g, is 807 μW cm^{-2}, corresponding to a normalized power density (ω_n) of 1.82 μW cm^{-2} K^{-2}. The inset image in Fig. 6g is a wearable display of the slot device. Also, a V_{oc} of 13.8 mV while wearing is shown in Supplementary Fig. 41. To verifying the accuracy of the performance test, we employ the formula $\rho = RA/l$, where ρ denotes the resistivity, A denotes the cross-sectional area, and l denotes the length, the σ of the device (σ_d) can be calculated to be ~925 S cm^{-1}, exhibiting 77% of the thin-film material, indicating a reasonable compatibility between our device and material performance. However, the internal resistance of silver paste and the interface resistance between the material and silver paste are the main factors affecting the σ_d. To verify the difference between the P of our device and the theoretical power in the structure, we employ a matched load power formula: $P_{max} = (\frac{V_{oc}}{R_{in}+R_{load}})^2 \times R_{load}$, where V_{oc} is calculated by $V_{oc} = n \times S \times \Delta T$ (n refers to the number of legs), where R_{in} refers to device internal resistance of the slotted device, and R_{load} refers to external resistance in the test circuit. The tested values represent 90% of the calculated values, indicating the maximum P of the device under this structure. Additionally, the test results, along with the theoretical predictions, are presented in Supplementary Fig. 42.

Apart from the slotted thin-film device, we also assembled a conventional horizontal four-leg TED for wearing as shown in Fig. 6h and Supplementary Fig. 43. Supplementary Figs. 44 and 45 exhibits that the P and V_{oc} closely match the theoretical values calculated for the design, with the maximum P of 115 nW at a ΔT of 28 °C. To verify the usability of the four-leg TED, we also adhered the device to the body surface and evaluated its voltage output under different motion states (Fig. 6i). Through these series of tests, the Ag_2Se thin-film-based device manufactured using the electron beam/solution method has been proven to have excellent durability and practical prospects. However, to achieve better performance output, reasonable optimization in design is still inevitable.

In this work, we designed highly oriented Ag_2Se thin films using the electron beam and solution immersion method, introducing a novel approach to controlling film anisotropy by adjusting the concentration of Se precursor to optimize its thermoelectric performance. Under selenization with a selenium content of 10 mmol, the electrical transport direction was steered away from the uneven charge distribution associated with the nearly parallel planes of (00 l) orientation. The combined effects of thin film anisotropy optimization, a small quantity of V_{Se}, and Ag nanoinclusions in the thin film resulted in an exceptionally high $S^2\sigma$ of 30.8 μW cm^{-1} K^{-2} at 343 K. The precisely controlled film thickness, crystallinity, and strong adhesion to the flexible polyimide substrate led to excellent flexibility and stability, with performance variation staying within 5% after 2000 bending cycles at a radius of just 5 mm. The films also exhibited high durability, maintaining over >90% of with power factor after six months. A slotted, wearable thermoelectric device was fabricated using the optimized thin films, achieving a V_{oc} of 27.1 mV, a P of 0.58 μW, and a ω of 807 μW cm^{-2} at a ΔT = 20 °C with a corresponding ω_n of 1.8 μWcm^{-2} K^{-2}. This research introduces a new method for controlling film orientation, with significant implications for high-performance, thin-film-based thermoelectrics.

https://doi.org/10.1038/s41467-025-56671-7

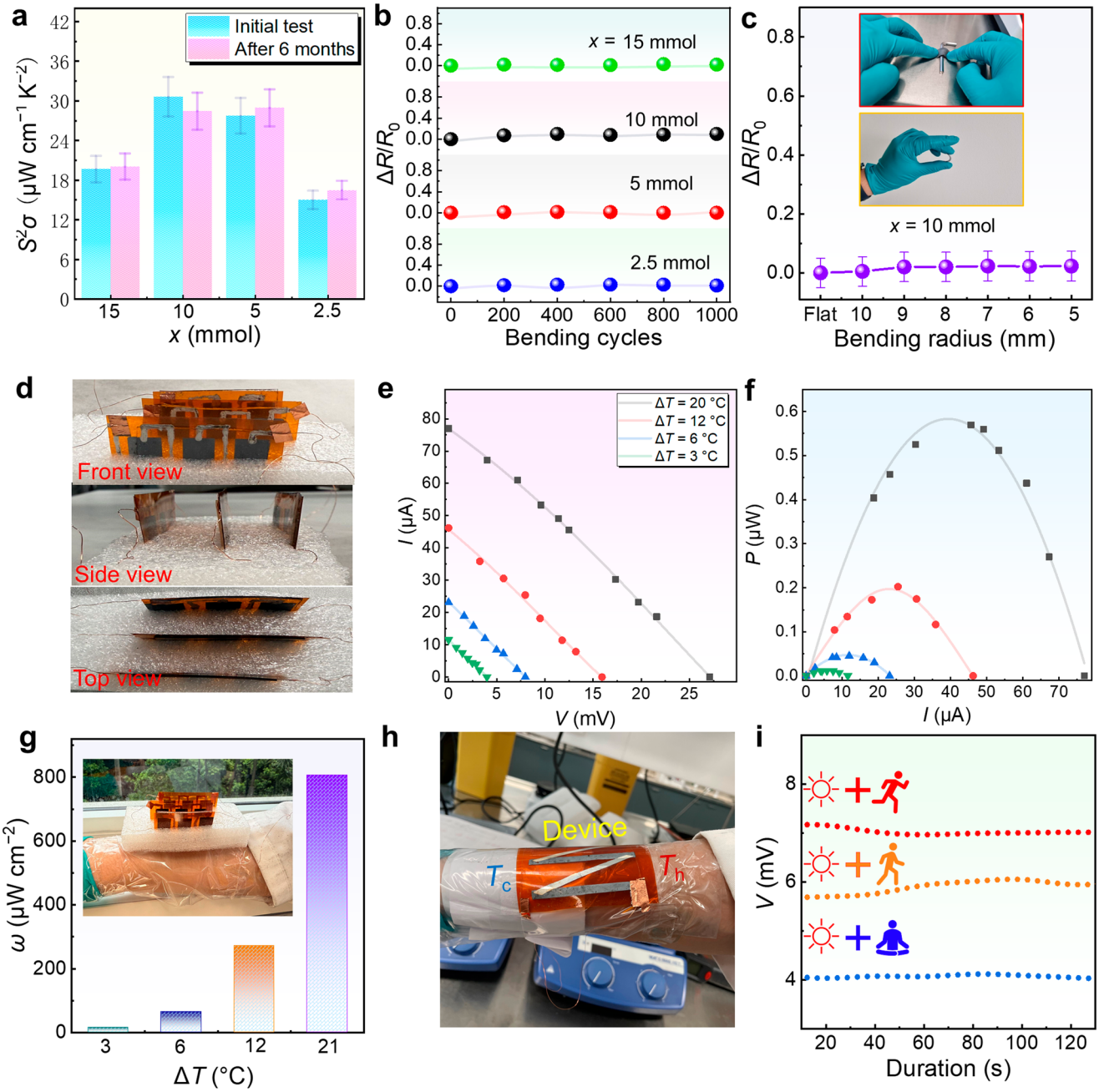

Fig. 6 | Durability and flexibility of Ag_2Se thin films and their device performance. a Durability testing results of thin films with different x (comparison of $S^2\sigma$ values before and after 6 months). Here, 5% error bar is employed. **b** Normalized resistance change ($\Delta R/R_0$) of thin films with different x as a function of bending cycle with a fixed bending radius r of 5 mm. **c** $\Delta R/R_0$ of Ag_2Se thin film with $x = 10$ mmol as a function of r under 200 bending cycles. The inset photos exhibit the high flexibility of thin films. Here, 5% error bar is employed. **d** Three views of slotted device including front view at the top, side view at the middle, and the top view at the bottom. **e** Relations between voltage (V)and current (I) at different ΔTs, as well as **f** relations between I and output power (P) at different ΔTs. **g** Determined power density (ω) at different ΔTs. The inset is the wearability demonstration of the slotted thin film TED. **h** Photograph demonstrating the wearability of the four-leg conventional horizontal TED. **i** Measured V of the four-leg device while being worn during sitting, walking, and running as a function of duration.

Methods

Materials synthesis

Pure Ag thin films were prepared on PI film using electron beam evaporation (PVD 75 E-beam, Kurt J. Lesker). A carbon crucible (1.167 inch top × 0.563 inch height × 0.093 inch wall thickness and 15-degree wall angle) was employed to contain Ag particles (purity 99.99%, Kurt J. Lesker), which were placed into the deposition chamber. The PI film (30 mm × 30 mm × 0.12 mm, Cole-Parmer) underwent a 15-min sonication in ethanol before being adhered to the deposition plate inside the chamber. The background pressure was maintained below 5×10^{-6} Torr. Ag deposition source parameters were set to I of 31 mA and V of 10 kV, with thickness controlled by a detector to approximately 500 nm. Subsequently, the Ag thin film, prepared via electron beam deposition, underwent selenization using a solution method. The solvent portion of the precursor, comprising 20 ml of water and 20 ml of ethanol, was precisely measured using a graduated cylinder and thoroughly mixed in a centrifuge tube. Se powder (100 mesh, 99.99%, Sigma Aldrich) was dissolved in a mixed solution of ethanol and water, in varying amounts: 15 mmol, 10 mmol, 5 mmol, 2.5 mmol, and 1.25 mmol. The

mixed solution also contained $Na_2S{\cdot}9H_2O$ (98%, Sigma Aldrich) in amounts of 60 mmol, 50 mmol, 20 mmol, 10 mmol, and 5 mmol, respectively. After soaking in the reaction for 20 min, the thin films were removed, and surface residue was washed with isopropanol and a small amount of water. After cleaning, the samples were placed into an oven (ACROSS international) and annealed at 180 °C for 10 h to obtain the Ag_2Se thin film samples for testing.

Characterizations

Grazing incident XRD analysis was conducted using a Rigaku Smart Lab instrument with CuKα radiation across an angular range of 20° to 60° in 0.02° increments to ascertain the crystal orientation of the Ag_2Se thin-film samples. XRD results were refined using TOPAS Pawley refinement, achieving a weighted profile p-factor (RWP) of 9.90 and a goodness of fit (GOF) of 1.17. XPS analysis was conducted using Kratos Axis Supra Photoelectron Spectroscopy. Morphological analysis, mapping, and composition assessment of the samples were performed using a JOEL 7001 F SEM. An EDS detector from Bruker, the EDS QUANTAX, was utilized for EDS analysis. Furthermore, lamina samples of Ag_2Se thin films were prepared using the FEI Scios FIB. The Cs-STEM (Hitachi HF5000) was employed for HAADF in STEM mode to conduct microanalysis of Ag_2Se thin film FIB samples.

Thermoelectric performance evaluation

The σ and S were measured using a Seebeck coefficient and electrical conductivity apparatus (ZEM-3). The D was determined using the alternative current method measurement system (RIKO Laser-PIT). The n and μ were investigated using a Van der Pauw Hall measuring instrument (CH-70, CH-magnetoelectricity Technology Co., Ltd., China) under a magnetic field up to 500 mT. The n and μ were determined by $n = 1/eR$ and $\mu = \sigma R$, respectively.

Data availability

The data generated in this study is provided in the Source Data file. Source data are provided with this paper.

References

1. Tian, R., Liu, Y., Koumoto, K. & Chen, J. Body heat powers future electronic skins. *Joule* **3**, 1399–1403 (2019).
2. Cao, T., Shi, X.-L. & Chen, Z.-G. Advances in the design and assembly of flexible thermoelectric device. *Prog. Mater. Sci.* **131**, 101003 (2023).
3. Snyder, G. J. & Toberer, E. S. Complex thermoelectric materials. *Nat. Mater.* **7**, 105–114 (2008).
4. Yang, Q. et al. Flexible thermoelectrics based on ductile semiconductors. *Science* **377**, 854–858 (2022).
5. Pei, Y. et al. Convergence of electronic bands for high performance bulk thermoelectrics. *Nature* **473**, 66–69 (2011).
6. Chen, S. & Ren, Z. Recent progress of half-Heusler for moderate temperature thermoelectric applications. *Mater. Today* **16**, 387–395 (2013).
7. Chen, W. et al. Nanobinders advance screen-printed flexible thermoelectrics. *Science* **386**, 1265–1271 (2024).
8. Tang, X., Li, Z., Liu, W., Zhang, Q. & Uher, C. A comprehensive review on Bi_2Te_3-based thin films: thermoelectrics and beyond. *Interdiscip. Mater.* **1**, 88–115 (2022).
9. Zheng, Z.-H. et al. Harvesting waste heat with flexible Bi_2Te_3 thermoelectric thin film. *Nat. Sustain.* **6**, 180–191 (2023).
10. Lu, Y. et al. Staggered-layer-boosted flexible Bi_2Te_3 films with high thermoelectric performance. *Nat. Nanotechnol.* **18**, 1281–1288 (2023).
11. Wei, T.-R., Qiu, P., Zhao, K., Shi, X. & Chen, L. Ag_2Q-Based (Q = S, Se, Te) silver chalcogenide thermoelectric materials. *Adv. Mater.* **35**, 2110236 (2023).
12. Zhu, M., Shi, X.-L., Wu, H., Liu, Q. & Chen, Z.-G. Advances in Ag_2S-based thermoelectrics for wearable electronics: progress and perspective. *Chem. Eng. J.* **475**, 146194 (2023).
13. Wang, H. et al. Synergetic enhancement of strength-ductility and thermoelectric properties of Ag_2Te by domain boundaries. *Adv. Mater.* **35**, 2302969 (2023).
14. Wu, H., Shi, X.-l, Duan, J., Liu, Q. & Chen, Z.-G. Advances in Ag_2Se-based thermoelectrics from materials to applications. *Energy Environ. Sci.* **16**, 1870–1906 (2023).
15. Lu, Y. et al. Nanoengineering approach toward ultrahigh power factor Ag_2Se/polyvinylpyrrolidone composite film for flexible thermoelectric generator. *Chem. Eng. J.* **485**, 149793 (2024).
16. Kleinhanns, T. et al. A route to high thermoelectric performance: solution-based control of microstructure and composition in Ag_2Se. *Adv. Energy Mater.* **14**, 2400408 (2024).
17. Ding, Y. et al. High performance n-Type Ag_2Se film on nylon membrane for flexible thermoelectric power generator. *Nat. Commun.* **10**, 841 (2019).
18. Jiang, C. et al. Ultrahigh performance of n-Type Ag_2Se films for flexible thermoelectric power generators. *ACS Appl. Mater. Interfaces* **12**, 9646–9655 (2020).
19. Chen, N. et al. High-performance thermoelectric silver selenide thin films cation exchanged from a copper selenide template. *Nanoscale Adv.* **2**, 368–376 (2020).
20. Mallick, M. M. et al. New frontier in printed thermoelectrics: formation of β-Ag_2Se through thermally stimulated dissociative adsorption leads to high *ZT*. *J. Mater. Chem. A* **8**, 16366–16375 (2020).
21. Zheng, Z.-H. et al. Achieving ultrahigh power factor in n-type Ag_2Se thin films by carrier engineering. *Mater. Today Energy* **24**, 100933 (2022).
22. Perez-Taborda, J. A., Caballero-Calero, O., Vera-Londono, L., Briones, F. & Martin-Gonzalez, M. High thermoelectric *zT* in n-Type silver selenide films at room temperature. *Adv. Energy Mater.* **8**, 1702024 (2018).
23. Hu, B. et al. High-performing flexible Mg_3Bi_2 thin-film thermoelectrics. *Adv. Sci.* **11**, 2409788 (2024).
24. Lei, Y. et al. Microstructurally tailored thin β-Ag_2Se films towards commercial flexible thermoelectrics. *Adv. Mater.* **34**, 2104786 (2021).
25. Hou, S. et al. Encapsulated Ag_2Se-based flexible thermoelectric generator with remarkable performance. *Mater. Today Phys.* **38**, 101276 (2023).
26. Ma, H. et al. Flexible Ag_2Se thermoelectric films enable the multifunctional thermal perception in electronic skins. *ACS Appl. Mater. Interfaces* **16**, 7453–7462 (2024).
27. Zheng, Z.-H. et al. Significantly (00*l*)-textured Ag_2Se thin films with excellent thermoelectric performance for flexible power applications. *J. Mater. Chem. A* **10**, 21603–21610 (2022).
28. Yang, D. et al. Flexible power generators by Ag_2Se thin films with record-high thermoelectric performance. *Nat. Commun.* **15**, 923 (2024).
29. Jia, L. et al. Optimization of power factor for a screen-printed silver selenide-based flexible thermoelectric film by hot pressing. *ACS Appl. Energy Mater.* **7**, 5721–5727 (2024).
30. Gao, J. et al. Thermoelectric flexible silver selenide films: compositional and length optimization. *iScience* **23**, 100753 (2020).
31. Li, X. et al. Exceptional power factor of flexible Ag/Ag_2Se thermoelectric composite films. *Chem. Eng. J.* **434**, 134739 (2022).
32. Liu, Y. et al. High performance Ag_2Se films by a one-pot method for a flexible thermoelectric generator. *J. Mater. Chem. A* **10**, 25644–25651 (2022).
33. Liu, Y. et al. Nanoengineering approach toward high power factor Ag_2Se/Se composite films for flexible thermoelectric generators. *ACS Appl Mater. Interfaces* **15**, 36587–36593 (2023).

34. Wang, J. et al. Tetragonal–Orthorhombic–Cubic phase transitions in Ag_2Se nanocrystals. *Chem. Mater.* **26**, 5647–5653 (2014).
35. Lee, J., Windus, T. L., Thiel, P. A., Evans, J. W. & Liu, D.-J. Coinage Metal–Sulfur Complexes: Stability on Metal(111) SURFACES AND IN THE GAS PHase. *J. Phys. Chem. C.* **123**, 12954–12965 (2019).
36. Luo, Y. et al. Enhanced thermoelectric performance in flexible sulfur-alloyed Ag_2Se thin films. *ACS Appl. Mater. Interfaces* **16**, 36620–36627 (2024).
37. Niu, J. et al. In-situ growth of high room temperature thermoelectric performance Ag_2Se thin films. *Mater. Lett.* **312**, 131662 (2022).
38. Zang, J. et al. Effect of post-annealing treatment on the thermoelectric properties of Ag_2Se flexible thin film prepared by magnetron sputtering method. *Res. Phys.* **45**, 106222 (2023).
39. Zhang, J. et al. High-performance thermoelectric flexible Ag_2Se-based films with wave-shaped buckling via a thermal diffusion method. *ACS Appl. Mater. Interfaces* **15**, 47158–47167 (2023).
40. Park, W., Park, S., Mun, Y., Lee, D. & Jang, K.-S. Effects of thickness on flexibility and thermoelectric performance of free-standing Ag_2Se films. *J. Ind. Eng. Chem.* **121**, 142–148 (2023).
41. Kumar, S., Battabyal, M., Sethupathi, K. & Satapathy, D. K. High-performance printed Ag_2Se/PI flexible thermoelectric film for powering wearable electronics. *ACS Appl. Mater. Interfaces* **16**, 40848–40857 (2024).
42. Chen, Y.-X. et al. Deviceization of high-performance and flexible Ag_2Se films for electronic skin and servo rotation angle control. *Nat. Commun.* **15**, 8356 (2024).
43. Zhang, M. et al. Scalable printing high-performance and self-healable Ag_2Se/terpineol nanocomposite film for flexible thermoelectric device. *Energy* **296**, 131232 (2024).
44. Liu, Y. et al. Fully inkjet-printed Ag_2Se flexible thermoelectric devices for sustainable power generation. *Nat. Commun.* **15**, 2141 (2024).
45. Yue, Y. et al. Solvothermal synthesis of micro-pillar shaped Ag_2Se and its thermoelectric potential. *Mater. Today Chem.* **39**, 102183 (2024).
46. Wang, H. et al. Flexible Porous Ag_2Se films: from freestanding inorganic films to inorganic-network/organic-skeleton thermoelectric generators. *Adv. Funct. Mater.* **35**, 2413605 (2025).
47. Gao, Q. et al. High power factor Ag/Ag_2Se composite films for flexible thermoelectric generators. *ACS Appl. Mater. Interfaces* **13**, 14327–14333 (2021).
48. Hou, S. et al. High performance wearable thermoelectric generators using Ag_2Se films with large carrier mobility. *Nano Energy* **87**, 106223 (2021).
49. Jiang, C. et al. Ultrahigh performance polyvinylpyrrolidone/Ag_2Se composite thermoelectric film for flexible energy harvesting. *Nano Energy* **80**, 105488 (2021).
50. Lee, D. et al. Substrate-Free Thermoelectric 25 μm-Thick Ag_2Se Films with High Flexibility and In-Plane *zT* of 0.5 at Room Temperature. *ACS Appl. Mater. Interfaces* **15**, 3047–3053 (2023).
51. Li, J., Liu, Y., Wang, Z., Chen, L. & Cai, K. Ultra-flexible self-supporting Ag_2Se/nylon composite films for wearable thermoelectric devices. *Compos. Part B-eng.* **265**, 110946 (2023).
52. Lu, Y., Liu, Y., Li, Y. & Cai, K. The influence of Ga doping on preparation and thermoelectric properties of flexible Ag_2Se films. *Compos. Commun.* **27**, 100895 (2021).
53. Lu, Y. et al. Ultrahigh power factor and flexible silver selenide-based composite film for thermoelectric devices. *Energy Environ. Sci.* **13**, 1240–1249 (2020).
54. Lu, Y. et al. Ultrahigh performance PEDOT/Ag_2Se/CuAgSe composite film for wearable thermoelectric power generators. *Mater. Today Phys.* **14**, 100223 (2020).
55. Sarkar, P. et al. Improved power factor in highly textured n-Type Ag_2Se flexible films. *ACS Appl. Electron Mater.* **5**, 1650–1659 (2023).
56. Wu, M. et al. Ultraflexible and high-thermoelectric-performance sulfur-doped Ag_2Se film on nylon for power generators. *ACS Appl. Mater. Interfaces* **14**, 4307–4315 (2022).
57. Saeidi-Javash, M. et al. Machine learning-assisted ultrafast flash sintering of high-performance and flexible silver–selenide thermoelectric devices. *Energy Environ. Sci.* **15**, 5093–5104 (2022).
58. Mallick, M. M., Franke, L., Rösch, A. G. & Lemmer, U. Shape-Versatile 3D thermoelectric generators by additive manufacturing. *ACS Energy Lett.* **6**, 85–91 (2021).
59. Li, Y. et al. Exceptionally high power factor Ag_2Se/Se/Polypyrrole composite films for flexible thermoelectric generators. *Adv. Funct. Mater.* **32**, 2106902 (2022).
60. Palaporn, D., Mongkolthanaruk, W., Faungnawakij, K., Kurosaki, K. & Pinitsoontorn, S. Flexible thermoelectric paper and its thermoelectric generator from bacterial cellulose/Ag_2Se nanocomposites. *ACS Appl. Energy Mater.* **5**, 3489–3501 (2022).
61. Yang, Z.-y et al. Ag_2Se/nylon self-supporting composite films for wearable photo-thermoelectric generators with high output characteristics. *J. Mater. Chem. A* **10**, 21080–21092 (2022).
62. Hou, S. et al. High-performance, thin-film thermoelectric generator with self-healing ability for body-heat harvesting. *Cell Rep. Phys. Sci.* **3**, 101146 (2022).
63. Xin, C. et al. Solution-processed flexible n-Type S-Doped Ag_2Se thermoelectric generators for near-ambient-temperature energy harvest. *Mater. Today Energy* **33**, 101266 (2023).
64. Hu, Q.-X. et al. SWCNTs/Ag_2Se film with superior bending resistance and enhanced thermoelectric performance via in situ compositing. *Chem. Eng. J.* **457**, 141024 (2023).
65. Xia, X. et al. Integrated, highly flexible, and tailorable thermoelectric type temperature detectors based on a continuous carbon nanotube fiber. *Small* **17**, 2102825 (2021).
66. Geng, J. et al. High power factor n-Type Ag_2Se/SWCNTs hybrid film for flexible thermoelectric generator. *J. Phys. D. Appl. Phys.* **54**, 434004 (2021).
67. Park, D., Lee, S. & Kim, J. Thermoelectric and mechanical properties of PEDOT:PSS-coated Ag_2Se nanowire composite fabricated *via* digital light processing based 3D printing. *Compos. Commun.* **30**, 101084 (2022).
68. Liang, J. et al. Crystalline structure-dependent mechanical and thermoelectric performance in $Ag_2Se_{1-x}S_x$ System. *Research* **2020**, 6591981 (2020).
69. Li, W. et al. Facile synthesis of cubic Ag/Ag_2O composites and its shape-dependent photo-catalytic activity examination. *J. Mater. Sci. Mater. Electron.* **30**, 5366–5374 (2019).
70. Konar, R. et al. Facile and scalable ambient pressure chemical vapor deposition-assisted synthesis of layered silver selenide (β-Ag_2Se) on Ag foil as a possible oxygen reduction catalyst in alkaline medium. *Electrochim. Acta* **370**, 137709 (2021).
71. Lin, Y. et al. Expression of interfacial Seebeck coefficient through grain boundary engineering with multi-layer graphene nanoplatelets. *Energy Environ. Sci.* **13**, 4114–4121 (2020).
72. Shen, J., Chen, Z., Zheng, L., Li, W. & Pei, Y. Single parabolic band behavior of thermoelectric p-type $CuGaTe_2$. *J. Mater. Chem. C.* **4**, 209–214 (2016).
73. Shi, X.-L., Zou, J. & Chen, Z.-G. Advanced thermoelectric design: from materials and structures to devices. *Chem. Rev.* **120**, 7399–7515 (2020).
74. Wei, J., Zhang, Q., Zhao, L., Hao, L. & Nie, Z. Effect of moisture on the thermoelectric properties in expanded graphite/carbon fiber cement composites. *Ceram. Int.* **43**, 10763–10769 (2017).

Acknowledgements

This work was financially supported by the Australian Research Council, HBIS-UQ Innovation Center for Sustainable Steel project, QUT Capacity

Building Professor Program, and AINSE Ltd. Early Career Researcher Grant (ECRG). The calculations were conducted in the Research Computing Centre at the University of Queensland, and the National Computational Infrastructure supported by the Australian Government. This work was enabled using the Central Analytical Research Facility hosted by the Institute for Future Environments at QUT.

Author contributions

Z.-G.C. and X.-L.S. supervised the overall experiments. T.C. designed the related experiments. B.H., W.C., L.-C.Y., Q.-Y.L., Q.Y., S.L., and W.-Y.L. prepared materials and measured the thermoelectric properties, designed device structures, fabricated devices, and measured the performance. T.C., X.-L.S., X.W., and Z.-G.C. analyzed the data. S. S. performed the device numerical simulation and M.L. conducted the DFT calculations. Q.L., T.T., J.M., and W.-D.L. discussed the results. T.C. X.-L.S. and Z.-G.C. wrote the manuscript with the help of all the authors.

Competing interests

The authors declare no competing interests.

Additional information

Supplementary information The online version contains supplementary material available at https://doi.org/10.1038/s41467-025-56671-7.

Correspondence and requests for materials should be addressed to Xiao-Lei Shi or Zhi-Gang Chen.

Peer review information *Nature Communications* thanks Rafiq Mulla, Hanhwi Jang, and the other, anonymous, reviewer(s) for their contribution to the peer review of this work. A peer review file is available.